Purely spatial coincidences of twin photons in parametric spontaneous down conversion.

Jean-Luc Blanchet, Fabrice Devaux, Luca Furfaro, and Eric Lantz*
Département d'Optique P.M. Duffieux,
Institut FEMTO-ST, UMR CNRS 6174,
Université de Franche-Comté, 16 route de Gray,
F-25030 Besançon Cedex, France

(Dated: January 25, 2010)

We have measured sub-shot-noise quantum correlations of spatial fluctuations in the far field image of the parametric fluorescence created in a type I BBO non linear crystal, either between opposite angular sectors (non degenerate configuration) or between opposite pixels (degenerate configuration). Imaging is performed at very low light level (0.2 photons per pixel) with an electron multiplying CCD camera, resulting in purely spatial coincidences between single photons when detecting on pixels. Experimental results overcome the standard quantum limit shot noise level without subtraction of the variance of the detection noise. We compare these experimental results with numerical results given by the quantum Green's function method, which is proved to have strong advantages over stochastic simulations.

PACS numbers: 42.50.Ar, 42.50.Dv, 42.50.Lc, 42.65.Lm

I. INTRODUCTION

Spontaneous down conversion (SPDC) occurs in a nonlinear crystal when a pump photon splits in a pair of signal and idler photons. Even if the number of pairs fluctuates, this relation is exact in the sense that, in the absence of input light at the signal and idler frequency, the difference between the signal and idler output photon numbers is zero in an ideal experiment. Heidmann *et al.* [1] showed that the spectrum of temporal fluctuations of the intensity difference between spatially monomode twin beams is below the standard shot noise level. Actually, the beams are entangled: the phases of the beams are also correlated at the quantum level, as shown by homodyne detection. If the two detectors do not intercept the whole beams, the correlation is reduced because for some pairs one photon is detected while the other is not intercepted. Because "intercepted" can be replaced by "detected" in the previous sentence, such insufficient size of a detector is exactly equivalent to a reduction of the quantum efficiency.

The situation is different for a strongly spatially multimode beam issued from a traveling wave amplifier: Brambilla *et al.* showed theoretically [2] that, for unity quantum efficiency, the variance of the signal-idler photon number difference goes to zero if the pixel size is much greater than the coherence area. These results were numerically confirmed either by stochastic simulations corresponding to Wigner formalism [3] or by using the quantum Green's function method [4]. Indeed, Boyer *et al.* studied temporal fluctuations of spatially broad-band twin beams obtained by four-wave mixing in a hot atomic vapor and showed that part of the beams larger than the coherence area exhibit sub-shot-noise intensity-differences [5], as well as entanglement [6], if detected with local oscillators shaped as the beams. These experiments demonstrated temporal entanglement of "subbeams" but did not consider fluctuation of spatial variables, like position or angle. Entanglement of such variables for beams [7] was demonstrated by combining TEM00 beams with a vacuum squeezed TEM01 beam and homodyne detection of temporal fluctuations [8]. On the other hand, Boyd *et al.* [9] demonstrated spatial entanglement of photon pairs in an image by varying the position of detectors in both the near and the far-field and recording temporal coincidences. Other spatial properties of twin photons have been extensively studied in the group of Boston [10] by recording temporal coincidences.

Though dealing with spatial aspects of multimode beams, all the experiments in the above references were devoted to the characterization of temporal fluctuations or temporal coincidences. However, patterns in an image are pure spatial information, without any time aspect, which are ultimately degraded by spatial fluctuations of quantum origin for very weak images [11]. Jedrkiewicz *et al.* [12] performed the first experimental demonstration of sub shot-noise behavior of spatial fluctuations of the signal-idler difference. They imaged SPDC issued from a type II BBO crystal onto a back illuminated CCD camera and showed that the value of the variance of the difference between signal-idler intensities on opposite pixels is below the shot noise level. However, this result was obtained by subtracting the variance of the readout noise, i.e. about 100 squared photoelectrons, from a measured variance of 110 squared photoelectrons. With a conventional CCD, diminishing the relative weight of the detection noise requires the acquisition of more intense im-

*Electronic address: eric.lantz@univ-fcomte.fr

ages and convincing results have been recently obtained without subtraction of the background noise [13], for intensities around 600 photons per pixel and a pump pulse duration in the *ns* range, in order to avoid excess noise due to the thermal character of SPDC [14].

We chose the opposite direction for obtaining sub-shot-noise correlations, without subtraction of the variance of the detector noise, by detecting single photons in low light level images with an electron multiplying CCD camera (EMCCD). In such cameras, the readout noise is rendered negligible by adding a register where the photoelectrons are multiplied before reading. Hence even a unique photon gives a signal that emerges from the read-out floor. However, the gain is stochastic, as in an avalanche photodiode, and it is not possible to assign a precise number of photons to each value of the output signal.It can be demonstrated [15] that dividing the output signal by the mean gain results in adding a Poisson detection noise having the same amplitude as the standard photon noise. This excess noise prevents any attempt to detect sub-shot noise correlations, at least without subtraction of the variance of the detection noise. On the other hand, detection of single photons by thresholding adds in principle no noise for high gain, even stochastic, and very low light level images. In practice, false detections occur, whose number can be minimized [16] by choosing an appropriate fluence (about 0.15 photon/pixel with our camera) and by adjusting the threshold. In these conditions, the variance of the detection noise is much smaller than the mean fluence and detection of sub-shot noise correlations becomes possible. We first studied [17] type I broad-band non-degenerate SPDC, and showed correlations between angular sectors, then added an interferential filter to obtain SPDC around degeneracy, in order to obtain correlations between opposite pixels [18]. We proved in this latter case spatial coincidences between individual photons. The aim of this paper is to present in more details these experimental results, especially those in the degeneracy configuration, and to add a discussion of the numerical methods that allow a comparison. In particular, we will show that usual stochastic simulations, based on the Wigner formalism, are not feasible in practice for intensities of the order of tenths of photons per pixel, while the Green's function method can be rendered less computational expensive than expected at a first sight. The paper is organized as follows. Section 2 deals with experimental results at degeneracy, while section 3 treats the broad-band configuration. Section 4 is devoted to numerical simulations and Section 5 concludes.

II. MEASUREMENT OF SUB-SHOT-NOISE CORRELATIONS BETWEEN PIXELS

The experimental setup is sketched in Fig.1. The pump pulse provided by the fourth harmonic (0.93 ps duration at 263.8 nm) of a Q-switched mode-locked Nd:Glass laser (Twinkle laser by Light Conversion Inc.) at a repetition rate of 33 Hz, illuminated a type I 7 x 7 x 4 mm^3 beta-barium-borate (BBO) nonlinear crystal. The far field image of the parametric fluorescence was formed in the focal plane of a lens by a back-illuminated EMCCD camera from Andor technology, (model iXon+ DU897-ECS-BV) with a quantum efficiency greater than 90 % in the visible range. The detector area is formed by 512 x 512 pixels, with a pixel size of 16 x 16 μm^2. We used a readout rate of 10 MHz at 14 bit and the camera was cooled at $-85\,^\circ$C. The exposure time was 33 ms and the EM gain was set to 1000. In these conditions, the read-out noise has a standard deviation of 46 electrons and the level of clock induced noise, i.e. generation of spurious electrons during the transfer, is of the order of $4\times 10^{-3} e^{-}/pixel$. A threshold set to 2.8 read-out noise standard deviations allows the number of false detections to be minimized [16]. To eliminate the residual UV, two dichroic filters with a nominal transmission of 95% at 527 nm were placed after the BBO crystal. To obtain degenerate parametric fluorescence, an interferential filter (IF)was placed after the dichroics, with a quantum efficiency greater than 90 % over a bandwidth of 20 nm, while broadband fluorescence was obtained simply by removing this filter. All the trajectory of the light after the dichroics and the filter was enclosed in a tube in order to avoid parasitic reflections. The energy of the 263.75 nm pump pulse was measured to 106 ± 38nJ. The total quantum efficiency is the product of the quantum efficiency of the EMCCD by the transmission of the optical elements after the crystal:

$$\eta_{tot} = \eta_{CCD} \times \eta_{opt} \times \eta_{IF} = 0.9 \times 0.68 \times 0.9 = 0.55 \quad (1)$$

η_{CCD} is given by the manufacturer and η_{opt} was measured. In particular, a transmission by the two dichroic filters of 80 % has been measured.

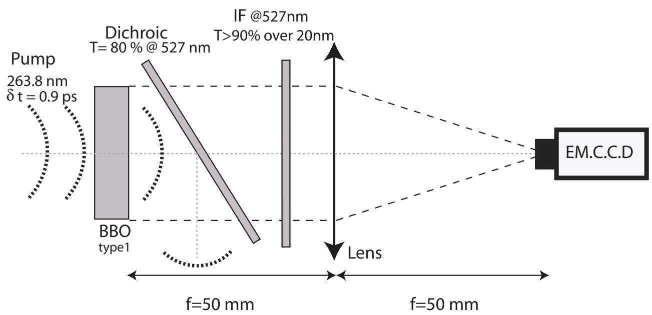

FIG. 1: experimental setup

Measurements at degeneracy were performed for a crystal orientation corresponding to collinear phase-matching. Fig. 2 shows a sum of 50 single shot images of parametric fluorescence recorded by the EMCCD. Unlike in a single image,the fluorescence disk is clearly visible. The mean level in the disk for one image, about 0.20 photon per pixel, has been chosen in order to minimize the number of false detections [16].

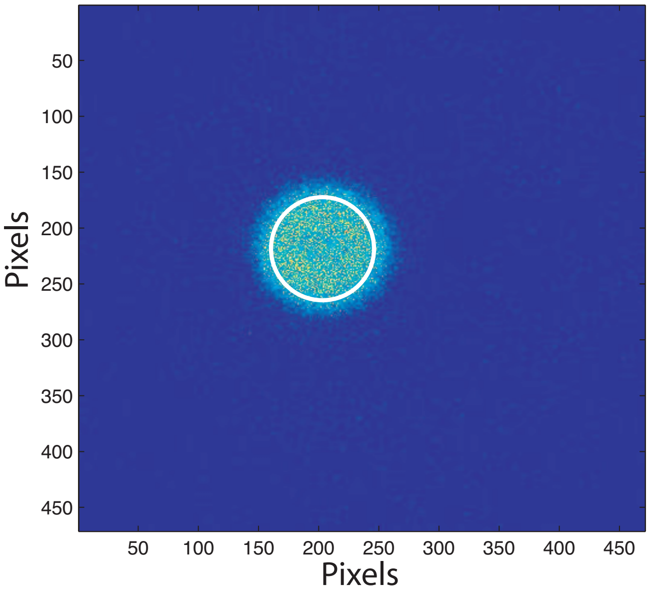

FIG. 2: Sum of 50 experimental images. The white circle delimits the area where the statistic is performed

We have measured the difference between the number of photons in opposite pixels, which should go to zero for a perfect detector, perfect degeneracy and negligible diffraction, i.e. for a coherence area much smaller than the pixel size [4]. This last condition is fulfilled here because of the wide illumination of the crystal : the measured pump width on the crystal (FWHM) is 3.2 mm. For pure spontaneous down conversion with negligible further amplification and a pump beam area smaller than the crystal section ($7 \times 7mm^2$ here), the down-converted beam has the same intensity profile as the pump beam. The width of the coherence area in the far field, 0.07 mrd (FWHM), is proportional to the inverse of the width of this beam [19] and is much smaller than the 0.32 mrd lateral size of the CCD pixel. Moreover the mean number of photons for one spatio-temporal mode is less than 10^{-2}, resulting in theoretical Bose-Einstein photon distribution [20] that is undistinguishable from a Poisson distribution. Indeed, the number of amplified temporal modes is approximately 40 [19] and the number of amplified spatial modes on a pixel is of the order of $(0.32/0.07)^2 \simeq 20$. To take into account the non uniform level of the electronic background over the detector area, this background is measured in darkness and subtracted from the SPDC images in the form of a mean square plane. Then, a thresholding procedure is applied on each image, in order to decide whether there is one or zero photoelectron on each pixel [16]. Note that it is not possible to distinguish the (rare) cases where two photoelectrons are present on one pixel. The variance of the difference between opposite pixels is then computed inside a circle containing N pixels where the level of SPDC is approximately constant. The center of this circle is determined by minimizing the variance of the difference

$$\sigma^2_{diff} = \frac{1}{N/2} \sum_{i=1}^{N/2} (n_i - n_{N-i})^2 \qquad (2)$$

with a numbering of the pixels ensuring that indices i an $N - i$ correspond to opposite pixels. The center determination must be performed with precision[14], at best with a resolution of half a pixel in order to keep the actual pixels with, in case, a unused crux : see Fig. 3. After this centering has been performed with physical pixels, statistics can be calculated using square blocks of pixels, called binned pixels.

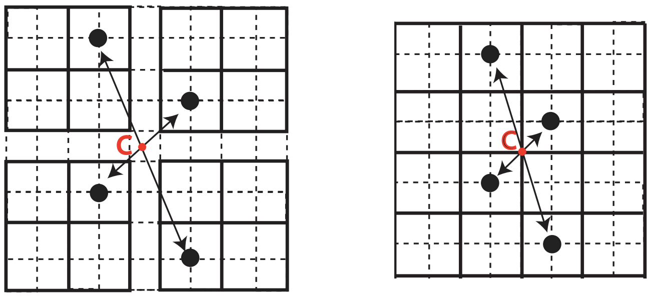

FIG. 3: centering for a 2×2 binning. Left : the best center corresponds to the center of a physical pixel. Right : the best center corresponds to the corner between four physical pixels.

It should be noted that subpixel centering algorithms exist [21] [22] and have been employed with good results in [13] but we have not used them in the presented results, in order to conserve a measurement of either zero or one photon per physical pixel. We have nevertheless verified that improvements of results provided by these methods do exist for our experimental results, but are weak because of the predominence of quantum noise in our low flux regime.

For perfect detection, sub-shot-noise correlations exist if σ^2_{diff} is smaller than twice the mean $n_{moy} = \frac{1}{N}\sum_{i=1}^{N}(n_i)$. However the measured variance of the photon number appears to be smaller than the mean photon number, while the equality is expected for a Poisson distribution. This phenomenon can be easily explained by taking into account the cases where two photoelectrons or more are accumulated in the same pixel. If μ is the true mean number of photoelectrons accumulated in one pixel, a thresholding procedure would give, in the absence of false detections, a measured mean m given by

$$m = 1 - p(0) = 1 - exp(-\mu) \qquad (3)$$

where $p(0)$ is the probability of detecting no photoelectron. The first equality expresses the fact that the thresholding procedure is unable to distinguish between one and more photoelectrons on one pixel, while the second equality reflects the Poisson distribution of photoelectrons. With the same hypotheses, the measured variance σ^2 is given by

$$\sigma^2 = m^2 p(0) + (1-m)^2(1-p(0)) = m(1-m) \quad (4)$$

Hence, the measured variance is smaller than the measured mean, because of the binary detection. On the other hand, the variance of the difference is affected in the same way as the variance by this effect. To cancel this artefact, the criterion for the detection of sub-shot-noise correlations becomes :

$$\frac{\sigma^2_{diff}}{m(1-m)} \leq 2 \quad (5)$$

Hence, the measured ratio σ^2_{diff}/n_{moy} must be multiplied by a correction coefficient $c = 1/(1-n_{moy})$ in order to be compared to the shot noise limit (SNL). If binned pixels are used, c must be estimated before binning, since thresholding is performed on the physical pixels.

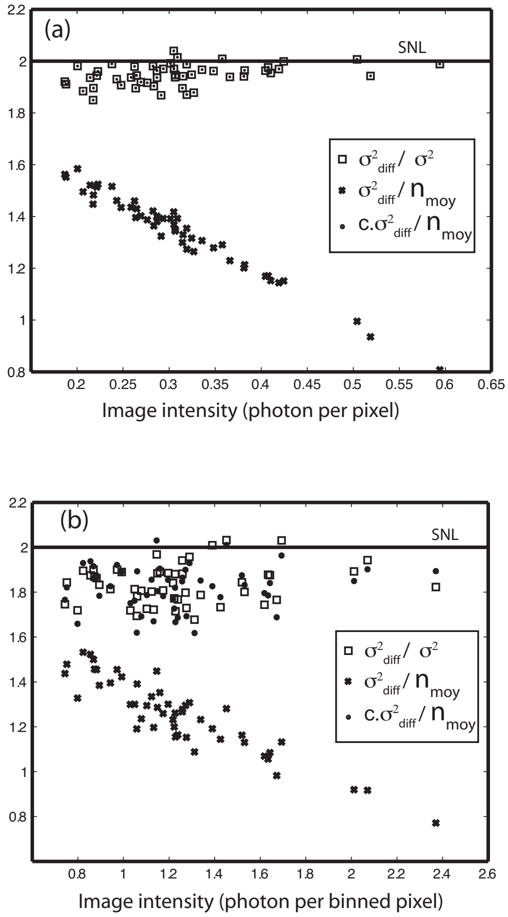

FIG. 4: Experimental results. Each point corresponds to a single shot measurement. (a): no binning. (b): 2×2 binning

Fig. 4 presents the measured ratios on 50 images, either without binning and with 4848 physical pixels in the statistics area or for 1212 blocks of 2×2 pixels. In the absence of binning, the corrected ratios r are almost exactly equal to the ratios of the variances $r' = \sigma^2_{diff}/\sigma^2$, meaning that the classical noise is negligible, while the corrected ratios are slightly different from the variance ratios for 2×2 binning, because of the smaller number of samples. In both cases, these ratios are clearly in the quantum regime. At 95% of confidence the results on individual images are :

$$r = c \times \frac{\sigma^2_{diff}}{n_{moy}} = 1.94 \pm 0.08 \quad (6)$$

$$r' = \frac{\sigma^2_{diff}}{\sigma^2_s} = 1.94 \pm 0.08 \quad (7)$$

for physical pixels and

$$r = c \times \frac{\sigma^2_{diff}}{n_{moy}} = 1.82 \pm 0.18 \quad (8)$$

$$r' = \frac{\sigma^2_{diff}}{\sigma^2_s} = 1.83 \pm 0.16 \quad (9)$$

for blocks of 2×2 pixels. In this latter case, the dispersion is doubled, because the number of pixels has been divided by 4. While the limits of the confidence interval for individual images attain the SNL, the averages of the estimators on the 50 images are well below the SNL:

$$< r > = 1.94 \pm \frac{0.08}{\sqrt{50}} = 1.94 \pm 0.01 \quad (10)$$

$$< r' > = 1.94 \pm \frac{0.08}{\sqrt{50}} = 1.94 \pm 0.01$$

for physical pixels and

$$< r > = 1.82 \pm \frac{0.18}{\sqrt{50}} = 1.82 \pm 0.02 \quad (11)$$

$$< r' > = 1.83 \pm \frac{0.18}{\sqrt{50}} = 1.83 \pm 0.02 \quad (12)$$

for blocks of 2×2 pixels.

To conclude this section, we have demonstrated pure spatial quantum correlations between opposite pixels of different sizes. For the smallest size, corresponding to the physical pixels, this correlation corresponds to spatial coincidences between individual photons, because the number of photons per pixel is either one or zero. However, though diffraction is negligible even for this pixel size, correlations are reduced because of imperfect centering, non perfect degeneracy and detector errors, as it will be shown in section 4. The best results have been obtained by grouping the pixels in 2×2 blocks.

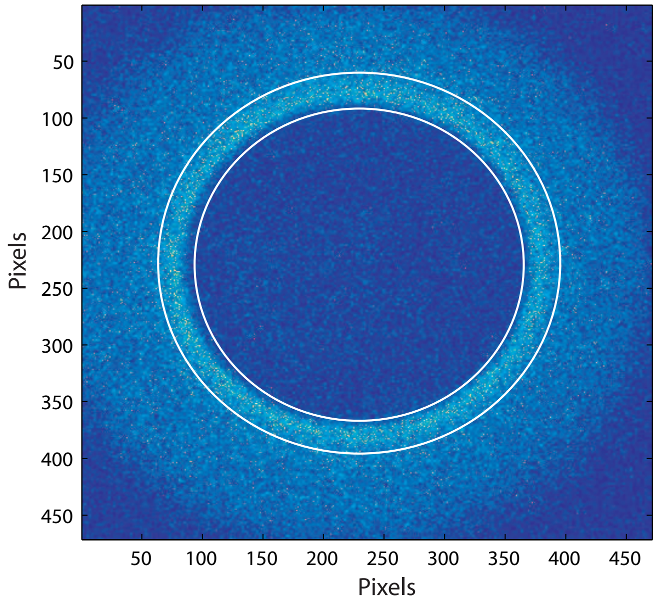

FIG. 5: Sum of 58 experimental images in pass-band configuration. The white circles delimit the area where the statistic is performed.

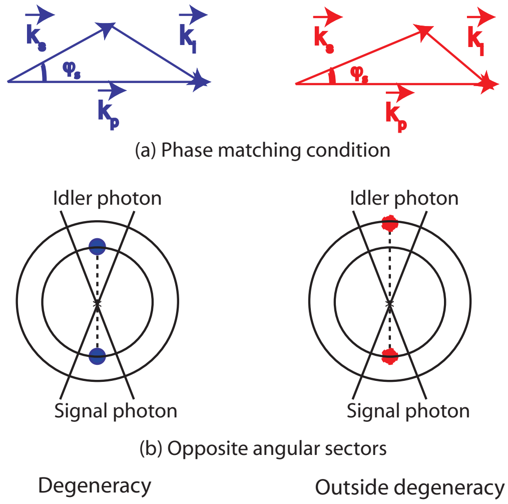

FIG. 6: a) Non collinear phase matching : $\vec{k}_{p,s,i}$ wave vectors of respectively pump, signal, idler. (b) Correlation between angular sectors. For non collinear phase matching, idler and signal form rings of different diameters.

III. MEASUREMENT OF SUB-SHOT-NOISE CORRELATIONS BETWEEN ANGULAR SECTORS

We now describe results obtained without chromatic filtering for a crystal orientation corresponding to non-collinear phase matching. Fig. 5 shows a sum of 58 single shot images in this configuration. For non degenerate wavelengths, the idler and signal fluorescence form rings of different diameter and the rings corresponding to different wavelengths add incoherently in the image. However, because of momentum conservation, each pair of twin photons emitted in the SPDC process, although not equidistant from the center of the pattern, lies along a diameter line, as shown in Fig. 6.

The SPDC image is divided in S=90 angular sectors and a number of photons n_i is determined in the intersection of each of these sectors with a ring encompassing the greatest part of the multimode SPDC. The center of this ring is determined in order to obtain the most regular distribution of light between sectors on the sum image. Note that only the pump beam experiences walk-off: the center of the SPDC ring does not correspond to the center of the pump beam, with no practical consequences since this pump beam is not detected. The size of a sector, 240 pixels, results from a compromise between effects of diffraction and not perfect centering, that are more sensitive for small sectors, and of the other classical noises (e.g. deterministic residual aberrations, see below) that predominate if the number of photons in a sector is too large. The symmetrical sector-pair correlation is evaluated by estimating the ratios r and r' defined in the preceding section. Fig.7 shows the experimental results for 58 single shot images with a mean comprised between 0.1 and 0.25 photon/pixel : each point corresponds to a single shot measurement with a statistics performed over the 90 sectors. Results can be summarized for the whole set of images as:

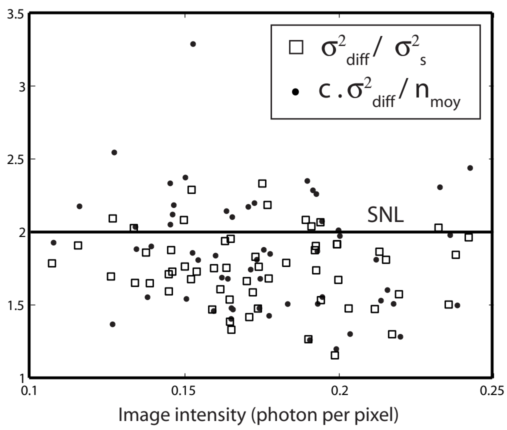

FIG. 7: Experimental results : each point corresponds to a single shot measurement.

$$r = c\frac{\sigma^2_{diff}}{n_{moy}} = 1.85 \pm 0.78\ ,\ r' = \frac{\sigma^2_{diff}}{\sigma^2_s} = 1.75 \pm 0.50 \quad (13)$$

For both values, the uncertainty range is centered on the average $\overline{r}$ or $\overline{r'}$ of the coefficients of the 58 images and the range width, i.e. ± 2 standard deviations of these 58 coefficients, gives a confidence of 95% for gaussian measurement errors. The dispersion of the measurements of r is mainly due to the measurement of σ^2_{diff} on a limited set of 90 pairs of sectors, giving a theoretical standard deviation for gaussian statistics $\sigma_{var} = (2/90)^{1/2}\sigma^2_{diff}$, hence a standard deviation on r, by neglecting the much smaller uncertainty on m: $\sigma_r = (2/90)^{1/2}\, r$, i.e a theoretical uncertainty range of ± 0.45. The other important source of dispersion of r comes from the fluctuations of the mean photon number from an image to another due to the fluctuations of the pump energy. Though some measurement values on individual images are greater than 2, in accordance with the uncertainty range of Eq.13, the mean coefficients for the 58 images are significantly smaller than 2 :

$$< r > \; = 1.85 \pm \frac{0.78}{\sqrt{58}} = 1.85 \pm 0.10 \qquad (14)$$

$$< r' > \; = 1.83 \pm \frac{0.50}{\sqrt{58}} = 1.83 \pm 0.07 \qquad (15)$$

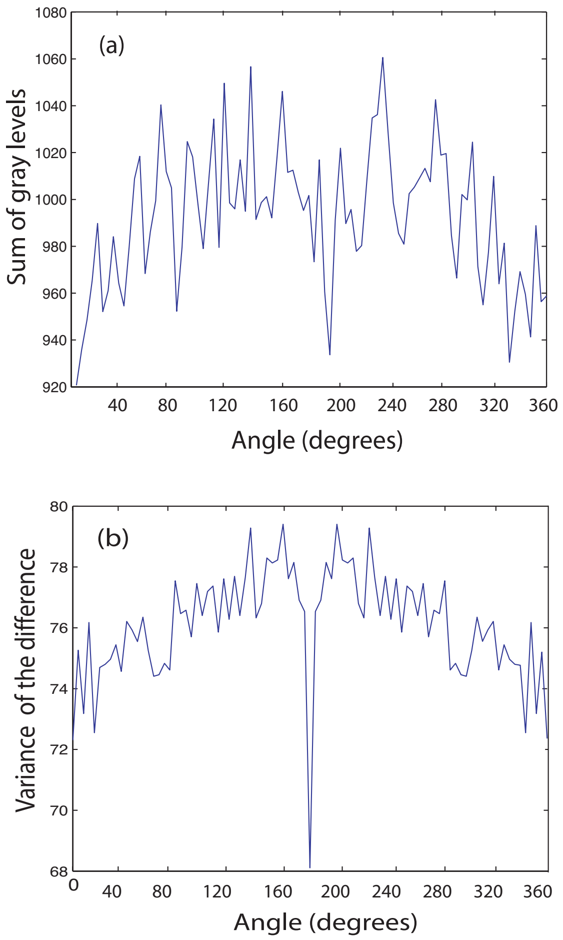

FIG. 8: (a) intensity (in sum of gray levels/sector) of the sum image versus the angular position of the sector. (b) Variance of the difference between sectors versus their angular separation.

We show in Fig.8b the evolution of the variance of the photon number difference between two non opposite sectors, versus their angular separation α :

$$\sigma^2_{diff,\alpha} = \frac{1}{S/2-1}\sum_{i=1}^{S/2}(n_i - n_{i+\frac{\alpha S}{2\pi}})^2 \qquad (16)$$

This variance increases when increasing α, because of some residual deterministic aberrations which are evidenced on Fig.8a, and falls abruptly for opposite sectors, because of quantum correlations. Nevertheless, these deterministic aberrations deteriorate the quantum correlations. An other deterioration comes from non collinear phase matching, in the cases where the signal ring is included in the detection area while the idler ring lies outside this area. If the detection was perfect, such situation could be avoided by extending the outer diameter of the detection ring. However, in practice, experimental results are worse because of the contribution of the detector noise in the low intensity part of this area.The other effects which deteriorate the theoretically perfect quantum correlations are detailed in the next section.

IV. NUMERICAL SIMULATIONS

A. Stochastic simulations

In the linear approximation, one can show that the Wigner distribution of the output field can be simulated by integrating the classical propagation equations starting from a stochastic field which has the phase-space distribution determined by the input field Wigner function. By averaging a great number of such simulations, one determines the expectation values of symmetrized operators. However, quantities measured in an experiment do not correspond to symmetrized operators but rather to normal ordering, so that correction terms must be added to the averages. First, the expectation of the photon number in pixel $\vec{r}$ is given by

$$\langle \hat{a}^{+}_{\vec{r}}\hat{a}_{\vec{r}}\rangle = \langle \alpha^*_{\vec{r}}\alpha_{\vec{r}}\rangle_{stoch} - \frac{1}{2} \qquad (17)$$

Similarly, the normally ordered photon number variance is obtained by subtracting $\frac{1}{4}$ to the stochastic variance.

To perform the Monte-Carlo numerical simulations, we proceed with the following steps [4]:

- For each temporal mode, we generate the stochastic input field with the appropriate phase-probability distribution corresponding to the vacuum field in the Wigner representation, i.e. for each pixel Gaussian white noise with zero mean and a random phase, such that $\langle \alpha^*_{\vec{r}}\alpha_{\vec{r}}\rangle_{stoch} = \frac{1}{2}$.
- The propagation of the stochastic field is then evaluated by integrating classical propagation equations, which are solved with a split-step algorithm.
- The fluences for each temporal mode are added at the output to obtain results corresponding to a single trajectory.

- The expectations of the symmetrically ordered operators are estimated by averaging the results over a great number of trajectories.

- All the expectation values in the normal ordering are finally obtained from these stochastic averages by applying the appropriate corrections.

The duration of a temporal mode is roughly equal to the inverse of the bandwidth of the SPDC, resulting for a pump pulse duration of $1ps$ in approximately a temporal mode per nm of bandwidth, i.e approximately 20 temporal modes for a bandwidth limited by the interferential filter, or 40 temporal modes in the broadband SPDC configuration (the other modes give light outside the statistics area). Each temporal mode must be simulated with its proper couple of wavelengths. The final fluence of the order of 0.15 photons/pixel is thus obtained by subtracting $40 \times \frac{1}{2}$ =20 photons/pixel from the averaged output. The variance σ^2_{before} of this fluence before corrections, obtained as the average of N trajectories, has a mean of the order $40 \times \frac{1}{4} = 10$ photons^2/pixel and obeys a gaussian statistics (χ^2 law with $40N$ degrees of freedom) and with a variance σ^4_{before}/N. Hence, if the physical variance, i.e the variance after corrections, is of the order of 0.15, a huge number of trajectories must be averaged to determinate σ^2_{diff} with a precision at 95% of confidence of, say, 10% :

$$\frac{\sigma^4_{before}}{N} = (0.05\,\sigma^2)^2 \Rightarrow N = \left(\frac{\sigma^2_{before}}{0.05\,\sigma^2}\right)^2 \simeq 1.8 \times 10^6 \tag{18}$$

This number has to be multiplied by the number of temporal modes. To conclude this subsection, stochastic simulations need a non acceptable huge number of runs to give a good precision, because of the low light level in the output image, resulting in a too high difference between the fluences in the corrected and the non corrected images.

B. Green's function method

In the undepleted pump approximation, equations of parametric amplification are linear and the output field on the pixel $\vec{r}$ can be described as the sum of contributions from all the pixels $\vec{r_1}$, multiplied by Green's function $G(\vec{r}, \vec{r_1})$. To take into account the non commuting character of the fields in their quantum description, two Green's functions $G(\vec{r}, \vec{r_1})$ and $H(\vec{r}, \vec{r_1})$ must be introduced [23]. Their numerical values are computed using a delta function successively on both quadratures corresponding either to a maximum amplification or a maximum deamplification as an initial condition in the classical propagation equation. The output quadrature fields obtained through the numerical propagation of this delta-like input functions are directly proportional to linear combinations of the Green's functions. It is then easy to deduce the actual value of G and H after the numerical propagation of a delta function centered at each point of the transverse plane. To summarize the anterior work [4], the Green's functions H and G can be numerically computed as linear combinations of output fields obtained by propagation of delta function input fields. The propagation of these input fields must be computed for each position in the output crystal plane and for both input quadratures. The knowledge of these Green's functions allows us to compute all the output covariance functions.

To describe the experiment, the number and the size of the pixels in the simulation must correspond to the actual CCD sensor. At a first glance, it means that we have to calculate G and H Green's functions for 2×512^2 input delta functions, giving for one input pixel (2 delta functions, one per quadrature) 2×512^2 output values (2 Green's functions G and H). This scheme seems not practicable, because of the half a million simulations and the 10^{11} output values. However, symmetries and negligible terms allow a considerable reduction of the computations. For example, an angular sector includes 240 pixels. To calculate σ^2_{diff} characterizing this sector, simulations must be performed for input Diracs on the pixels of the sector plus a border 2 pixels wide, to take into account diffraction, and for input Diracs on an opposite area of the same dimensions, to retrieve signal-idler correlations. Hence approximately 2000 propagations of a field of 512×512 pixels must be performed and it is necessary to keep in memory only the results for $\vec{r}$ inside the sector or its opposite. This number is even considerably reduced in the degenerate case, because a binned pixel and its border include less than 100 physical pixels. The numbers above correspond to one temporal mode and must be multiplied by the number of these modes that give a significant contribution. To conclude this paragraph, the Green's function method appears the only one that allows the computation of quantum covariances for very low fluxes corresponding to photon counting detection.

C. Results

Four types of cause deteriorate the ideal perfect signal-idler correlation when considering opposite areas. First, the idler photon is detected in a coherence area around the exact opposite position of the detection of the signal photon, because of diffraction. This effect will be quantified by simulations involving only one temporal mode corresponding to degeneracy and oversampling in the far field. Second, the center of a physical pixel or the corner between four pixels does not correspond exactly to the symmetry center of the far-field image. Third, twin photons correspond to non degenerate frequencies, resulting in a non collinear phase matching scheme and non opposite locations in the far-field, see Fig.6. The Green's function allows us to quantify this effect, by using a sufficient number of temporal modes, with for each a specific sampling in the image space (near field) in order to obtain an uniform sampling in the far-field corresponding to the actual CCD sensor. Fourth, the imperfect detection by the camera leads to the loss of some photons and to the detection of spurious photoelectrons that do not correspond to actual photons. We present in the following results including successively these four types of error.

To quantify diffraction effects, we have to take into account the actual dimensions of the illuminated crystal and of the pump beam in the near field,while the sampling step in this near field must correspond to the entire phase matching bandwidth in the far field. By using 2048×2048 samples, both requirements are fulfilled, with 4×4 samples corresponding to one physical pixel of the camera in the far-field. Even for the smallest measurement area, i.e one physical pixel, the effect of diffraction appears to be weak: $r < 4 \times 10^{-2}$, because the coherence area is sufficiently smaller than the physical pixel. Hence, the other effects will be simulated with 512×512 samples, i.e a sample length equal to a fourth of the crystal transversal size, in order to keep computation times reasonable and to obtain in the far field an equal size between the sample in the simulations and the physical pixel. Diffraction effects will be nevertheless taken into account by using a pump beam diameter smaller than its actual diameter, in order to retrieve the same value of r as with 2048×2048 samples.

Centering is physically performed with a resolution of half a pixel, in order to avoid interpolation (see section 2). The maximum difference between the actual center and the center used in calculations of section 2 is therefore 0.25 pixel, if the actual center is determined without error. Fig.9 shows the evolution of r with this difference, in the case of no binning and of 2×2 binning. For the maximum theoretical shift of 0.25 pixel, r attains half the SNL if no binning is performed and twice less for 2×2 binning. r becomes negligible for greater binning, in particular in the case of the angular sectors of section 3.

Fig.9 shows also the difference between a strict degeneracy and the experiment described in section 2, where the SPDC is rendered narrow-band by a 20 nm wide filter. For perfect centering and without binning, r equals 0.4 for this multimode light. Actually, this value depends notably of the position of the opposite pixels that are used for the simulation: if the pair of pixels is close to the center of the far-field fluorescence disk, there is almost no degradation due to the multimode character of the SPDC, as shown in Fig.10: involved angles are small and the locations for different wavelengths, though not exactly opposite, are shifted of far less than one pixel. However, the shift increases linearly with the distance between both pixels, resulting in a linear increase of r. Actually, using a smaller statistics area (maximum distance from the center of 20 pixels instead of 40) induces a diminution of the experimental value of r: 1.93 instead of 1.94 found in Eq.11, but with a greater dispersion between images because of the smaller number of pixels available for the statistics. Note that an error in centering diminishes the effect of non perfect degeneracy because the asymmetry due to different wavelengths compensates in part the asymmetry due to imperfect centering : see the points for a high centering error in Fig.9. All the points in this figure have been obtained for twin pixels distant of 20 pixels from the center, i.e a middle value of this distance.

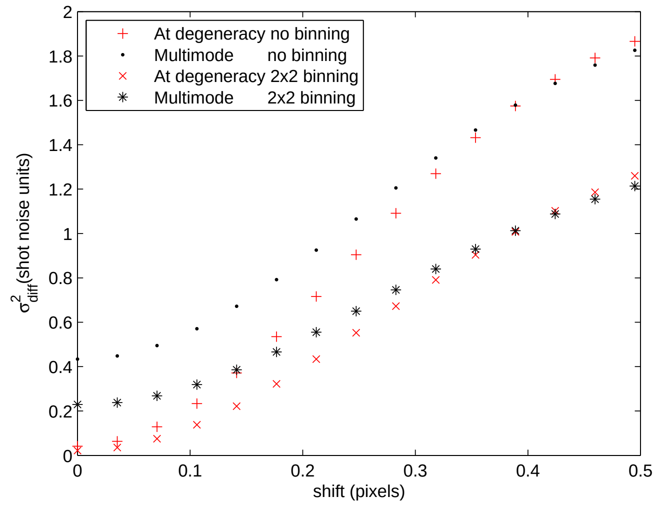

FIG. 9: Variance of the signal-idler difference versus the shift between the actual and the used center. The values in abscissa correspond to a shift along a diameter and to a shift of the same value in the orthogonal direction.The distance between the twin pixels and the center is 20 pixels

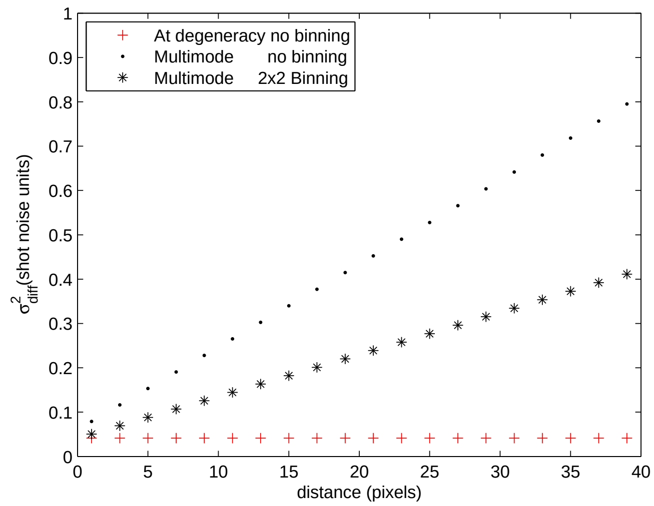

FIG. 10: Variance of the signal-idler difference versus the distance between the twin pixels and the center.

In actual measurements, r is computed by using different distances between twin pixels and without knowing the actual error on the center position. To take into account all the parameters, we have repeated the simulation for multimode SPDC with random values of the centering errors between 0 and 0.25 on both axes and random positions of the twin pixels inside the disk. We obtain $r_{perfect} = 0.93$ for perfect detection. We have then computed with our model of EMCCD camera[16] the probability p_1 of detecting only one photon on one pixel when opposite pixels receive either 0 or twin photons (ideal correlation before detection) for a detected photon mean m (see Eq.3) equal to 0.20, in agreement with the average of experimental results. The variance σ^2_{diff} after detection can then be computed as :

$$\sigma^2_{diff} = r_{perfect} \times \sigma^2 + p_1 \times (1 - r_{perfect}/2) \tag{19}$$

where σ^2 is computed with Eq.4. We obtain as final result for one physical pixel without binning:

$$r = c\frac{\sigma^2_{diff}}{m} = 1.47 \tag{20}$$

A part of the remaining difference between experiment ($r = 1.94$) and simulation ($r = 1.47$) is due to deterministic aberrations, visible on Fig. 8(a). However, this part is weak in the case of correlations between single pixels, because the quantum noise is predominent for a fluence smaller than 1 photon/pixel, and the origin of the discrepancy between simulation and experimental results is not clear. Note however that parametric amplifiers are often described in quantum optics by introducing an "excess noise" factor [24], whose origin comes from distortions in the pump wavefront.

In the case of a 2×2 binning, the experimental and simulated ratios become respectively $r = 1.82$ and $r = 1.29$ while, for angular sectors, they become $r = 1.75$ and $r = 1.33$. Note that, because of the greater number of photons in an angular sector, the deterministic aberrations induce an increase of r of about 0.1, that is no more negligible.

V. CONCLUSION

In conclusion, we have experimentally demonstrated in the photon-counting regime that opposite spatial fluctuations of spontaneous down conversion radiation are correlated in the quantum regime with a variance of the photon numbers between opposite areas below the shot-noise level. This conclusion holds close to degeneracy for opposite pixels as well as for broad-band SPDC for opposite angular sectors. In the case of physical pixels, purely spatial coincidences have been demonstrated, because the fluence of 0.2 photon/pixel corresponds to either zero or one photon on the pixel. These experimental results are supported by numerical simulations based on the Green's function method, that has been proved to have strong advantages on stochastic simulations for such a low photon flux.

[1] A. Heidmann, R. J. Horowicz, S. Reynaud, E. Giacobino, C. Fabre, and G. Camy, Phys. Rev. Lett. **59**, 2555 (1987).

[2] E. Brambilla, A. Gatti, L. Lugiato, and M. Kolobov, Eur. Phys. J. D **15**, 127 (2001).

[3] E. Brambilla, A. Gatti, M. Bache, and L. A. Lugiato, Phys. Rev. A **69**, 023802 (2004).

[4] E. Lantz, N. Treps, C. Fabre, and E. Brambilla, European Physical Journal D **29**, 437 (2004).

[5] V. Boyer, A. M. Marino, and P. D. Lett, Physical Review Letters **100**, 143601 (2008).

[6] V. Boyer, A. M. Marino, R. C. Pooser, and P. D. Lett, Science **321**, 544 (2008).

[7] M. T. L. Hsu, W. P. Bowen, N. Treps, and P. K. Lam, Physical Review A (Atomic, Molecular, and Optical Physics) **72**, 013802 (2005).

[8] K. Wagner, J. Janousek, V. Delaubert, H. Zou, C. Harb, N. Treps, J. F. Morizur, P. K. Lam, and H. A. Bachor, Science **321**, 541 (2008).

[9] J. C. Howell, R. S. Bennink, S. J. Bentley, and R. W. Boyd, Phys. Rev. Lett. **92**, 210403 (2004).

[10] D. V. Strekalov, A. V. Sergienko, D. N. Klyshko, and Y. H. Shih, Phys. Rev. Lett. **74**, 3600 (1995).

[11] A. Mosset, F. Devaux, and E. Lantz, Physical Review Letters **94**, 223603 (2005).

[12] O. Jedrkiewicz, Y.-K. Jiang, E. Brambilla, A. Gatti, M. Bache, L. A. Lugiato, and P. Di Trapani, Phys. Rev. Lett. **93**, 243601 (2004).

[13] G. Brida, L. Caspani, A. Gatti, M. Genovese, A. Meda, and I. R. Berchera, Physical Review Letters **102**, 213602 (2009).

[14] E. Brambilla, L. Caspani, O. Jedrkiewicz, L. A. Lugiato, and A. Gatti, Physical Review A (Atomic, Molecular, and Optical Physics) **77**, 053807 (2008).

[15] J. Hynecek and T. Nishiwaki, IEEE Transactions on Electron Devices **50**, 239 (2003).

[16] E. Lantz, J.-L. Blanchet, L. Furfaro, and F. Devaux, MNRAS **386**, 2262 (2008), 0803.1420.

[17] J.-L. Blanchet, F. Devaux, L. Furfaro, and E. Lantz, Physical Review Letters **101**, 233604 (2008).

[18] J. Blanchet, E. Lantz, L. Furfaro, and F. Devaux, CLEO/Europe-EQEC, ICM Munich, Germany (14-19 June 2009).

[19] F. Devaux and E. Lantz, European Physical Journal D **8**, 117 (2000).

[20] A. Mosset, F. Devaux, G. Fanjoux, and E. Lantz, European Physical Journal D **28**, 447 (2004).

[21] L. Oriat and E. Lantz, Patt. Recogn **31**, 761 (1998).

[22] L. Caspani, O. Jedrkiewicz, E. Brambilla, and A. Gatti, Journal of Modern Optics **55**, 2025 (July 2008).

[23] N. Treps and C. Fabre, Phys. Rev. A **62**, 033816 (2000).

[24] A. Ourjoumtsev, R. Tualle-Brouri, J. Laurat, and P. Grangier, Science **312**, 83 (2006).